

Alias-free 4D Gaussian Splatting

Zilong Chen¹, Huan-ang Gao², Delin Qu⁴, Haohan Chi², Hao Tang⁵, Kai Zhang^{1,†}, Hao Zhao^{2,3,†}

¹Tsinghua Shenzhen International Graduate School, Tsinghua University

²Institute for AI Industry Research (AIR), Tsinghua University

³Beijing Academy of Artificial Intelligence, BAAI ⁴Fudan University

⁵Peking University [†]Corresponding author

Abstract

Existing dynamic scene reconstruction methods based on Gaussian Splatting enable real-time rendering and generate realistic images. However, adjusting the camera’s focal length or the distance between Gaussian primitives and the camera to modify rendering resolution often introduces strong artifacts, stemming from the frequency constraints of 4D Gaussians and Gaussian scale mismatch induced by the 2D dilated filter. To address this, we derive a maximum sampling frequency formulation for 4D Gaussian Splatting and introduce a 4D scale-adaptive filter and scale loss, which flexibly regulates the sampling frequency of 4D Gaussian Splatting. Our approach eliminates high-frequency artifacts under increased rendering frequencies while effectively reducing redundant Gaussians in multi-view video reconstruction. We validate the proposed method through monocular and multi-view video reconstruction experiments. Ours project page: <https://4d-alias-free.github.io/4D-Alias-free/>

1. Introduction

Reconstructing dynamic scenes from monocular or multi-view videos has garnered significant attention due to its wide applications in augmented reality and virtual reality [16, 23, 39, 44, 46, 47, 51]. In addition to methods based on neural radiance fields (NeRFs) [2, 8, 14, 27, 29, 36, 38, 53, 57], 3D Gaussian Splatting (3DGS) [11, 22, 23] has emerged as a key approach for dynamic scene reconstruction, owing to its ability to render high-quality novel views in real-time. Recent advancements have extended 3DGS to the 4D domain, primarily through two approaches. The first approach employs 4D Gaussians in the spatiotemporal domain [9, 30, 54], computing Gaussian attributes across different time frames. The second approach models scene dynamics by deforming Gaussians over time [3, 21, 32, 42, 50, 55]. Both methods require the acquisition of 3DGS Gaussian representations at time t be-

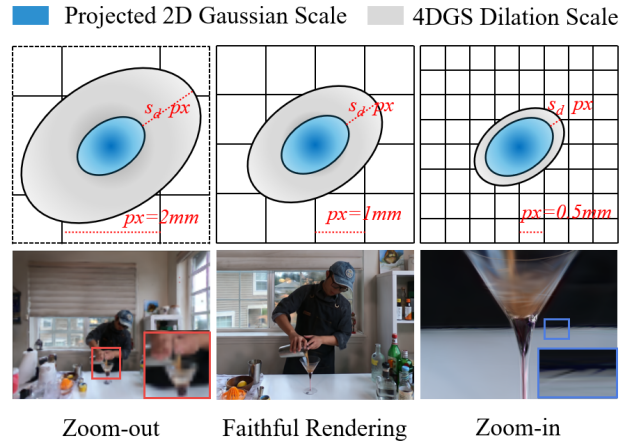


Figure 1. Similar to 3DGS [23], 4DGS undergoes substantial dilation when the sampling rate is lowered and experiences erosion along with high-frequency artifacts when the sampling rate is increased. This occurs because changes in resolution alter the effective pixel size while the Gaussian scale remains fixed, causing a mismatch between the Gaussian scale and the filter dilation scale, compounded by the absence of a maximum sampling frequency constraint in 4DGS.

fore rendering, with the distinction lying in the way Gaussian distributions over time are learned. We refer to both approaches collectively as 4DGS.

When the camera focal length or object-camera distance changes, altering the sampling rate, 4D Gaussian Splatting (4DGS) exhibits significant artifacts due to Gaussian scale mismatch caused by the 2D dilation filter, a known issue in 3DGS that persists in 4DGS. The 2D dilation filter expands Gaussians in screen space. As rendering resolution changes, pixel size varies while the Gaussian remains fixed, disrupting the dilation-to-Gaussian scale ratio and introducing severe artifacts, as shown in Fig. 1. Additionally, existing 4DGS methods lack constraints on Gaussian frequency. Especially in multi-view video reconstruction, modeling object motion with Gaussian movement is challenging, leading to redundant Gaussians. These small redundancies generate high-frequency artifacts when the sampling rate increases. However, incorporating the 3D smoothing filter

from 3DGS [56] into monocular video reconstruction methods [55] to constrain 4DGS frequency results in a decline in reconstruction quality. Our analysis shows that Gaussian properties, such as position and scale, change over time in 4DGS. A fixed dilation scale can make imperceptible small Gaussians visible and distort the scale ratio of anisotropic Gaussians, limiting 4DGS’s ability to capture spatio-temporal variations, as shown in Fig. 3. To address the above issues, we first derive the maximum sampling frequency formula for 4DGS based on the Nyquist-Shannon Sampling Theorem [35, 40], and propose a more flexible 4D scale-adaptive filter. Our key insights are twofold: first, we avoid dilating overly small Gaussians to prevent invisible Gaussians from becoming visible; second, when a Gaussian’s scale in a given dimension is smaller than or close to the dilation scale, a fixed dilation scale alters the scale ratio between dimensions, leading to anisotropic changes in the Gaussian. The 4D scale-adaptive filter adjusts the dilation scale within a certain range by computing the ratio of Gaussian scales before and after temporal changes, preserving the dimensional proportions after dilation and reducing the impact of filtering on Gaussian anisotropy, as shown in Fig. 3. Additionally, we propose a scale loss to constrain the Gaussian’s own scale, as filtering errors become more significant when the Gaussian scale is smaller than the filter scale. By distributing constraints between the filter and the Gaussian scale, we reduce the minimum dilation scale of the filter. While constraining the maximum frequency of 4DGS, we introduce the 2D Mip filter [56] to address the Gaussian scale mismatch in 4DGS.

In summary, we make the following contributions:

- We propose a maximum sampling frequency calculation method for 4DGS, from which we introduce the 4D scale-adaptive filter and scale loss to flexibly constrain the frequency of 4DGS, while incorporating the 2D Mip filter [56] for a general anti-aliasing solution in 4DGS.
- We integrate our method into the monocular video reconstruction algorithm D3DGS [55], demonstrating the superiority of the 4D scale-adaptive filter, which improves rendering quality at various resolutions without sacrificing full-resolution reconstruction quality.
- We integrate our method into the multi-view video reconstruction algorithm 4D Gaussian [50], where constraining the maximum sampling frequency of 4DGS effectively reduces redundant Gaussians, improves reconstruction quality, and eliminates high-frequency artifacts when increasing the sampling rate, as shown in Fig. 2.

2. Related Works

Dynamic 3D Gaussians: In recent years, 3D Gaussian Splatting (3DGS) [23, 25, 26, 53] has achieved remarkable progress in novel view synthesis, enabling real-time rendering at high-definition resolutions. Unlike ray tracing,



Figure 2. We trained all models on single-scale images (full resolution) and rendered images at different resolutions by adjusting the focal length. When the sampling rate changes, 4D Gaussians[50] exhibit strong artifacts, which our method effectively eliminates.

3DGS explicitly represents a scene as a set of 3D Gaussians and utilizes rasterization for rendering. Recent advancements have extended 3DGS to 4D, primarily following two approaches. The first employs 4D Gaussians in the spatiotemporal domain [9, 30, 54], computing Gaussian attributes across different time frames. This approach achieves high visual quality and real-time performance in multi-view video reconstruction. However, its limited accuracy in modeling Gaussian motion introduces significant redundancy, making it less effective for monocular reconstruction. The second approach models scene dynamics by deforming Gaussians over time [3, 7, 21, 32, 42, 50, 55], enabling precise motion estimation while maintaining a compact representation. This method is well-suited for both monocular and multi-view video reconstruction.

Anti-Aliasing in Neural Rendering: Aliasing is a common issue in computer graphics, arising when rendering frequency changes abruptly, leading to visual artifacts. Existing anti-aliasing techniques can be categorized into super-sampling and pre-filtering. The former increases the sampling rate to reconstruct high-frequency details in the scene [1, 12, 15, 17, 33, 48], while the latter mitigates aliasing by applying filters to suppress high-frequency components [10, 18, 34, 45, 49, 58]. In neural rendering, NeRF-based methods [4, 6, 19, 31] achieve effective anti-aliasing in static scenes, while DMiT extends pre-filtering to dynamic NeRFs, enabling aliasing suppression in dynamic scenes. 3DGS [23] suffers from severe artifacts when the dilation scale of the 2D dilation filter deviates from the intrinsic scale of Gaussian primitives during rendering. SA-GS [43] addresses this issue with a scale-adaptive 2D filter and integrates super-sampling but lacks robust

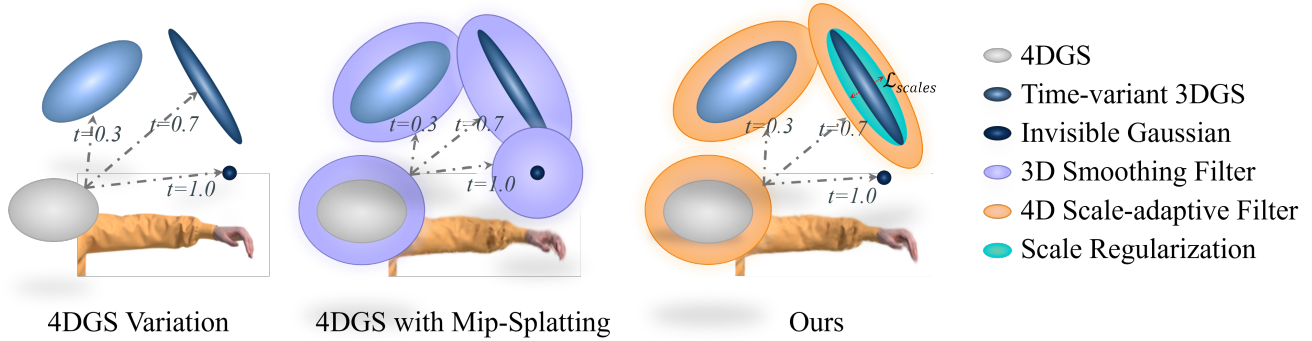


Figure 3. The fixed dilation scale used by the 3D smoothing filter proposed in Mip-Splatting [56] can inadvertently render imperceptible Gaussians with extremely small scales visible in 4DGS, and may alter the scale ratios among Gaussian dimensions, affecting Gaussian anisotropy. We present Alias-free-4DGS, which leverages a 4D Scale-adaptive Filter and Scale Regularization to jointly constrain the maximum sampling frequency of 4DGS. This reduces the filter’s minimum dilation scale and avoids significant filtering errors when Gaussian scales are much smaller than the filter’s dilation scale. Moreover, our 4D Scale-adaptive Filter masks out imperceptible Gaussians and adapts the dilation scale using the ratio of Gaussian scales before and after changes in the current time frame, thus mitigating the filter’s impact on Gaussian anisotropy. Alias-free-4DGS effectively eliminates artifacts that arise from varying sampling frequencies without compromising reconstruction quality.

anti-aliasing when increasing the sampling rate. Mip-Splatting [56] employs a hybrid filtering mechanism to suppress high-frequency components in both 2D and 3D Gaussians, achieving anti-aliasing. However, its fixed dilation scale limits flexibility, reducing its ability to preserve fine details and capture spatiotemporal variations in 4DGS, ultimately degrading reconstruction quality.

3. Preliminaries

3D Gaussian Splatting: Previous work [24, 58] proposed representing a 3D scene as a collection of scaled 3D Gaussian primitives and using volume splatting for image rendering. The geometry of each Gaussian primitive is defined in world coordinates by its opacity $\alpha_k \in [0, 1]$, center position $\mathbf{p}_k \in \mathbb{R}^{3 \times 1}$, and covariance matrix $\Sigma_k \in \mathbb{R}^{3 \times 3}$:

$$\mathcal{G}_k(\mathbf{x}) = e^{-\frac{1}{2}(\mathbf{x}-\mathbf{p}_k)^T \Sigma_k^{-1}(\mathbf{x}-\mathbf{p}_k)} \quad (1)$$

For optimization, the covariance matrix Σ_k is decomposed as $\Sigma_k = RSS^T R^T$, where R is a rotation matrix represented by a quaternion $r \in SO(3)$, and S is a scaling matrix represented by a 3D vector \mathbf{s} . The 3D Gaussians can be projected onto 2D and rendered for each pixel using the following 2D covariance matrix Σ'_k :

$$\Sigma'_k = J V \Sigma_k V^T J^T \quad (2)$$

Here, J denotes the Jacobian of the affine approximation of the projective transformation, and V represents the view matrix, which transitions coordinates from world space to camera space. By omitting the third row and column of Σ'_k , we obtain a 2D covariance matrix Σ_k^{2D} in ray space. We use G_k^{2D} to refer to the corresponding scaled 2D Gaussian. Finally, 3DGS [24] uses spherical harmonics to model

the view-dependent color c_k and renders the image via alpha blending according to the depth order of the primitives, which is $1, \dots, K$:

$$c(x) = \sum_{k=1}^K c_k \alpha_k G^{2D} k(x) \prod_{j=1}^{k-1} (1 - \alpha_j G_j^{2D}(x)) \quad (3)$$

4D Gaussian Splatting: The common approach for modeling dynamic scenes in both monocular and multi-view videos [50, 55] involves decoupling 4D Gaussians into 3D Gaussians and a deformation field. During the warm-up phase, a set of static Gaussians $G(p, r, s, \alpha)$ is first trained. Subsequently, the deformation field learns the changes in position Δp , rotation Δr , and scale Δs based on the Gaussian’s position p over time t . The deformed 3D Gaussians $G(p + \Delta p, r + \Delta r, s + \Delta s, \alpha)$ are then used for rendering. The 3D Gaussians and deformation network are optimized jointly through the fast backward pass by tracking accumulated α values, together with the adaptive control of the Gaussian density.

Filter: To avoid issues such as 2D Gaussians being smaller than one pixel after projection onto screen space, 3DGS employs a 2D dilation filter for low-pass filtering:

$$G_k^{2D}(x) = e^{-\frac{1}{2}(x-p_k)^T (\Sigma_k^{2D} + \sigma_s I)^{-1} (x-p_k)} \quad (4)$$

where I is a 2D identity matrix and σ_s is a scalar dilation hyperparameter. Mip-Splatting[56] replaces the 2D dilation filter with a 2D mip filter, effectively mitigating aliasing and dilation issues:

$$G_k^{2D}(x)_{mip} = \sqrt{\frac{|\Sigma_k^{2D}|}{|\Sigma_k^{2D} + \sigma_s I|}} e^{-\frac{1}{2}(x-p_k)^T (\Sigma_k^{2D} + \sigma_s I)^{-1} (x-p_k)} \quad (5)$$

Additionally, in MIP-splatting, a 3D smoothing filter is applied to limit the maximum sampling frequency of the Gaussians, thereby eliminating high-frequency artifacts that arise when increasing the sampling rate:

$$G_k(x)_{reg} = \sqrt{\frac{|\Sigma_k|}{|\Sigma_k + \frac{\sigma_s}{\hat{\nu}_k^2} \cdot I|}} e^{-\frac{1}{2}(x-p_k)^T (\Sigma_k + \frac{\sigma_s}{\hat{\nu}_k^2} \cdot I)^{-1} (x-p_k)} \quad (6)$$

$\hat{\nu}_k$ is the maximal sampling rate for primitive k .

4. Methods

4.1. Max Sampling for 4D Gaussian

Given the distance d between the Gaussian element and the camera, and the camera’s focal length f , it is straightforward to compute the sampling interval \hat{T} and the sampling frequency $\hat{\nu}$ of the Gaussian element:

$$\hat{T} = \frac{1}{\hat{\nu}} = \frac{d}{f} \quad (7)$$

To determine the maximum sampling frequency $\hat{\nu}$ for a single Gaussian element k , we minimize the ratio $\frac{d}{f}$. Let N denote the total number of cameras, the maximum sampling frequency can be determined as:

$$\frac{1}{\hat{\nu}_k} = \min_{n \in \{1, \dots, N\}} \left(\left\{ \mathbb{1}_n(p_k(t)) \cdot \frac{d_n(t)}{f_n(t)} \right\}_{t=1}^T \right) \quad (8)$$

Typically, $f_n(t)$ is fixed at a constant interval, and $p_k(t) = p_k + \Delta p_k(t)$. We approximate the depth $d_n(t)$ using the center of the primitive $p_k(t)$. The function $\mathbb{1}_n(p_k(t))$ acts as an indicator function that assesses the visibility of a primitive. Equation Eq. (8) provides a clear and intuitive formulation for calculating the maximum sampling frequency of the 4D Gaussian. However, the computational cost associated with evaluating $\Delta p_k(t)$ within the 4D Gaussian framework is substantial. When T is large, recalculating the maximum sampling frequency by iterating over all $\Delta p_k(t)$ values at each step can significantly extend the training duration. Consequently, we propose an approximate method to compute the maximum sampling frequency of the 4D Gaussian more efficiently.

During the warm-up phase and the early stage of training the deformation field, we use the initial positions of the Gaussian basis functions p_k to compute the rough minimum sampling interval \hat{T}_k :

$$\hat{T}_k = \min \left(\left\{ \mathbb{1}_n(p_k) \cdot \frac{d_n}{f_n} \right\}_{n=1}^N \right) \quad (9)$$

Once the deformation field stabilizes, we employ a momentum-based update method to learn a more accurate

sampling interval \hat{T}_k :

$$\hat{T}_k = (1 - \lambda_v) \cdot \hat{T}_k + \lambda_v \cdot \min \left(\hat{T}_k, \frac{d_n(t)}{f_n(t)} \right) \quad (10)$$

$\hat{\nu}_k$ is the reciprocal of \hat{T}_k . Note that although $d_n(t)$ still requires the computation of $\Delta p_k(t)$, due to the need to iterate over calculations in Eq. (10), we can directly get $d_n(t)$ during training in CUDA, as $d_n(t)$ is computed during the CUDA rendering process, making the overhead of Eq. (10) negligible.

4.2. 4D Scale-adaptive Filter

We introduce the 4D Scale-adaptive Filter at the maximum sampling frequency $\hat{\nu}_k$ of the 4D Gaussian primitive k . This approach is based on two considerations: First, the 4D Gaussian primitive k may be invisible at a specific time t , necessitating the avoidance of dilation at that time. Second, the 4D Gaussian models variations in scene information through scale changes Δs . When $s_t = s + \Delta s(t)$ in a given dimension becomes smaller than or approaches the dilation factor $\frac{\sqrt{\sigma_s}}{\hat{\nu}_k}$, fixed-scale dilation can distort the scale ratio between dimensions. The 4D Scale-adaptive Filter primarily adjusts the dilation coefficient based on scale variations, thereby flexibly constraining the frequency of the 4D Gaussian. First, the proportional change in the dilation coefficient, ρ_{adapt} , is computed according to the scale variation ratio:

$$\rho_{\text{adapt}} = \text{clip} \left(\frac{s_t^2}{s^2}, \rho_{\min}, \rho_{\max} \right) \quad (11)$$

The dilation coefficient is then updated for the visible Gaussian using ρ_{adapt} . The minimum dilation ratio ρ_{\min} constrains the Gaussian’s maximum frequency, while the maximum dilation ratio ρ_{\max} expands the dilation scale of enlarged dimensions within a certain range to preserve the dimensional scale ratio before and after dilation, mitigating the impact of filtering on Gaussian anisotropy.

$$\sigma_{\text{adapt}} = \begin{cases} \rho_{\text{adapt}} \cdot \sigma_s & \text{if } s_t^2 \geq \rho_{\text{thre}} \cdot \frac{\sigma_s}{\hat{\nu}_k^2}, \\ \epsilon \cdot \sigma_s & \text{otherwise.} \end{cases} \quad (12)$$

To prevent imperceptible Gaussians from becoming visible, we assign a minimal dilation scale ϵ to Gaussians with scales below a threshold. Filtering is then applied based on σ_{adapt} :

$$G_k(x, t)_{4D} = \sqrt{\frac{|\Sigma_k(t)|}{|\Sigma_k(t) + \frac{\sigma_{\text{adapt}}}{\hat{\nu}_k^2} \cdot I|}} e^{-\frac{1}{2}(x-p_k(t))^T \left(\Sigma_k(t) + \frac{\sigma_{\text{adapt}}}{\hat{\nu}_k^2} \cdot I \right)^{-1} (x-p_k(t))} \quad (13)$$

Methods	PSNR \uparrow					SSIM \uparrow					LPIPS _v \downarrow				
	Full Res.	1/2 Res.	1/4 Res.	1/8 Res.	Avg.	Full Res.	1/2 Res.	1/4 Res.	1/8 Res.	Avg.	Full Res.	1/2 Res.	1/4 Res.	1/8 Res.	Avg.
D-NeRF [37]	28.01	28.37	29.49	28.94	28.70	0.935	0.947	0.951	0.947	0.944	0.065	0.052	0.063	0.064	0.062
TiNeuVox [13]	31.24	32.12	32.55	30.50	31.60	0.962	0.969	0.975	0.966	0.968	0.059	0.045	0.035	0.046	0.046
K-Planes-H [14]	27.26	27.67	27.97	27.92	27.61	0.955	0.954	0.953	0.949	0.952	0.062	0.056	0.054	0.063	0.059
K-Planes-E [14]	26.80	27.18	27.58	27.34	27.23	0.951	0.949	0.948	0.941	0.947	0.069	0.065	0.064	0.068	0.067
Tensor4D [41]	25.25	25.67	26.04	25.15	25.49	0.932	0.934	0.938	0.921	0.931	0.101	0.093	0.071	0.050	0.079
4DGS [50]	30.13	30.36	30.84	30.63	30.49	0.963	0.966	0.968	0.967	0.966	0.048	0.042	0.042	0.038	0.042
D3DGS [55]	32.40	32.60	32.96	32.76	32.68	0.976	0.978	0.979	0.979	0.978	0.032	0.027	0.027	0.025	0.028
DMiT [52]	34.15	35.04	35.81	36.09	35.27	0.980	0.984	0.987	0.988	0.985	0.029	0.020	0.014	0.010	0.019
Ours	36.99	38.72	39.61	38.96	38.57	0.982	0.987	0.99	0.992	0.988	0.025	0.012	0.008	0.008	0.013

Table 1. Multi-scale Training and Multi-scale Testing on the D-NeRF dataset [37]. Our approach achieves state-of-the-art performance in most metrics.

Methods	PSNR \uparrow					SSIM \uparrow					LPIPS _v \downarrow				
	Full Res.	1/2 Res.	1/4 Res.	1/8 Res.	Avg.	Full Res.	1/2 Res.	1/4 Res.	1/8 Res.	Avg.	Full Res.	1/2 Res.	1/4 Res.	1/8 Res.	Avg.
D3DGS [55]*	38.30	32.48	26.63	22.35	29.94	0.986	0.975	0.932	0.857	0.937	0.017	0.016	0.035	0.072	0.035
D3DGS [55] - Dilation	35.45	35.64	34.07	31.47	34.16	0.977	0.980	0.979	0.973	0.977	0.030	0.022	0.028	0.054	0.034
2D Mip Filter [56]	38.45	38.20	35.61	32.42	36.17	0.985	0.988	0.986	0.980	0.985	0.018	0.011	0.012	0.019	0.015
Mip-Splatting _{4D} [56]	37.76	38.02	36.15	33.29	36.31	0.984	0.987	0.987	0.983	0.985	0.020	0.011	0.011	0.017	0.015
Ours	38.39	38.40	35.93	33.81	36.64	0.985	0.988	0.987	0.984	0.986	0.017	0.011	0.011	0.016	0.014

Table 2. Single-scale Training and Multi-scale Testing on the D-NeRF dataset [37]. All methods are trained on full-resolution images and evaluated at full resolution and three progressively lower resolutions, simulating zoom-out effects. Our approach preserves high-quality rendering at reduced resolutions while maintaining reconstruction fidelity at full resolution. * denotes models that we retrained.

4.3. Scale Regularization

Our intuition is to minimize the filter’s dilation scale by distributing it between the filter and the Gaussian’s scale constraint. We introduce the scale loss to jointly regulate the maximum sampling frequency of the 4D Gaussian using the 4D Scale-Adaptive Filter:

$$\mathcal{L}_{\text{scales}} = \sum_k \left(\left(\rho_{\min} \frac{\sigma_s}{\tilde{\nu}_k^2} - s_k(t) \right)^2 M_1 \right) \quad (14)$$

where $s_k(t) = s_k + \Delta s_k(t)$ represents the scale of primitive k at time t . Here, M_1 is an indicator function that activates when the scale satisfies $\rho_{\text{thre}} \cdot \frac{\sigma_s}{\tilde{\nu}_k^2} < s_k(t) < \rho_{\min} \cdot \frac{\sigma_s}{\tilde{\nu}_k^2}$.

4.4. Optimization

Similar to [50, 55], we first optimize the static Gaussians during the initial 3000 iterations as a warm-up phase, and then jointly optimize both the Gaussians and the deformation field. The training process is supervised by a combination of color loss and scale loss, formulated as:

$$\mathcal{L} = \mathcal{L}_{\text{color}} + \lambda_1 \cdot \mathcal{L}_{\text{scales}} \quad (15)$$

where $\mathcal{L}_{\text{color}}$ aligns with the coda base that integrates our filtering mechanism.

5. Experiments

We first present the implementation details of our method. We then evaluate its performance on the monocular video reconstruction dataset, D-NeRF [37], and the multi-view video reconstruction dataset, Neural 3D Video Dataset (N3DV) [28]. Finally, we discuss the limitations of our approach.

5.1. Implementation

We integrated our method into two state-of-the-art reconstruction frameworks: **D3DGS** [55], specialized for monocular video reconstruction, and **4DGaussians** [50], a deformation-based multi-view approach. Both the 2D Mip filter [56] and the 4D scale-adaptive filter were employed. Parameter settings followed their respective baselines, except for the densification threshold τ_g in **D3DGS**, which was adjusted to 0.0006. To maintain consistency with Mip-Splatting [56], we set $\sigma_s = 0.2$. For a fair generalization assessment, we used uniform settings of $\rho_{\min} = 0.2$ and $\rho_{\max} = 5$ across both frameworks, ensuring that the minimum effective Gaussian range approximated one pixel (defined as three times the Gaussian scale). When the rendering sampling rate decreases, we increase ρ_{\min} by multiplying it by the square of the ratio between the current and initial sampling rates, strictly capping it at 1. This adjustment is crucial, as a lower ρ_{\min} reduces the dilation scale, leading to a loss of Gaussian blurring on high-frequency information at lower sampling rates. To counteract this effect, we apply corresponding adjustments during rendering. The threshold ρ_{thre} was task-dependent, set to 0.05 for D3DGS and 5×10^{-6} for 4DGaussians. Additionally, we set $\lambda_v = 0.2$ and $\lambda_1 = 0.1$. Notably, in 4DGaussians, $\mathcal{L}_{\text{scales}}$ was computed using an average based on M_1 .

5.2. Evaluation on D-NeRF dataset

Multi-scale Training and Testing: Following previous works [5, 20, 52], we downsample images from the D-NeRF dataset by factors of 2, 4, and 8 to obtain multi-scale observations, adjusting focal lengths accordingly based on perspective projection. This setup facilitates a comprehensive



Figure 4. Single-scale Training and Multi-scale Testing on the D-NeRF dataset [37]. All methods are trained at full resolution and evaluated at various lower resolutions to simulate zoom-out effects. D3DGS [55] exhibits noticeable blurring and inflation artifacts at lower resolutions. Integrating Mip-splatting [56] mitigates inflation but introduces local reconstruction distortions, such as the deformation observed in the hand region (first row). In contrast, our method preserves the reconstruction quality of D3DGS while maintaining more realistic visual fidelity at lower resolutions.

	PSNR \uparrow				SSIM \uparrow				LPIPS \downarrow				$ \mathcal{G} $
	1x Res.	2x Res.	4x Res.	Avg.	1x Res.	2x Res.	4x Res.	Avg.	1x Res.	2x Res.	4x Res.	Avg.	
4DGaussian [50]	31.87	26.52	23.82	27.40	0.941	0.849	0.793	0.861	0.066	0.196	0.296	0.186	106K
2D Mip Filter [56]	32.79	29.63	27.94	30.12	0.964	0.904	0.849	0.906	0.041	0.140	0.248	0.143	74K
Mip-Splatting _{4D} [56]	33.47	30.51	29.31	31.10	0.966	0.916	0.880	0.921	0.040	0.138	0.237	0.138	68K
Ours	33.30	30.45	29.27	31.01	0.966	0.916	0.881	0.921	0.040	0.138	0.238	0.139	67K

Table 3. **Single-Scale Training and Multi-Scale Testing on the N3DV Dataset** [28]. All methods are trained at 1x and evaluated at 1x, 2x, and 4x, with higher sampling rates simulating zoom-in effects. While our method slightly underperforms Mip-Splatting [56] at the training resolution due to reduced lighting sensitivity, it achieves comparable or superior results at higher sampling rates. Additionally, constraining the frequency of 4DGS reduces the number of Gaussians $|\mathcal{G}|$ and enhances reconstruction quality.



Figure 5. **Single-Scale Training and Multi-Scale Testing on the N3DV Dataset [28]**. All models are trained on images downsampled by a factor of four and rendered at full resolution to simulate zoom-in and moving-closer effects. Our method effectively eliminates high-frequency artifacts and produces more complete object shapes compared to Mip-Splatting.

	PSNR \uparrow				SSIM \uparrow				LPIPS \downarrow			
	1x Res.	2x Res.	4x Res.	Avg.	1x Res.	2x Res.	4x Res.	Avg.	1x Res.	2x Res.	4x Res.	Avg.
D3DGS [55]*	39.69	30.15	27.37	32.40	0.990	0.959	0.936	0.962	0.008	0.033	0.061	0.034
2D Mip Filter [56]	40.568	36.104	33.827	36.833	0.990	0.981	0.967	0.979	0.008	0.025	0.048	0.027
Mip-Splatting _{4D} [56]	40.29	36.26	34.02	36.86	0.990	0.982	0.969	0.98	0.008	0.024	0.049	0.027
Ours w/o \mathcal{L}_{scales}	40.402	36.124	33.872	36.80	0.990	0.982	0.968	0.98	0.008	0.024	0.048	0.027
Ours	40.61	36.36	34.07	37.01	0.991	0.982	0.969	0.981	0.008	0.023	0.048	0.026

Table 4. Single-scale Training and Multi-scale Testing on the D-NeRF dataset [37]. All methods are trained on the smallest scale (1x) and evaluated across three scales (1x, 2x, and 4x), with evaluations at higher sampling rates simulating zoom-in effects. * denotes models that we retrained.

anti-aliasing evaluation by computing metrics across scales, as summarized in Tab. 1. Our method consistently outperforms all prior approaches across all metrics, including DMiT [52], which utilizes the Mipmapped Tri-Plane representation.

Single-scale Training and Multi-scale Testing: Following [43, 56], we train on full-resolution images and render at multiple scales (1x, 1/2, 1/4, and 1/8) to simulate zoom-out effects. Given the absence of publicly available benchmarks for 4D Gaussian Splatting in this context, we reproduce D3DGS [55] by replacing its 2D dilated filter with a

2D Mip filter [56]. Additionally, we adapt Mip-Splatting to 4DGS by introducing our proposed 4D frequency computation method in place of the original. To assess the effectiveness of our approach, we compare it against these implementations. Notably, our *4D Scale-adaptive Filter* can be configured to match the Mip-Splatting-based 4DGS implementation under specific parameters while offering greater flexibility. Quantitative comparisons are presented in Tab. 2. Although Mip-Splatting demonstrates good anti-aliasing capabilities, it reduces the reconstruction quality of D3DGS at full resolution. Qualitative comparisons in Fig. 4

Method	PSNR \uparrow	SSIM \uparrow	LPIPS _v \downarrow
Mip-Splatting _{4D} [56]	37.76	0.984	0.020
Mip-Splatting _{4D} [56] + M	38.20	0.985	0.018
Mip-Splatting _{4D} ($\rho_{min} \cdot \sigma_s$)[56] + M	38.32	0.985	0.017
Ours w/o \mathcal{L}_{scales}	38.47	0.986	0.017
Ours	38.39	0.985	0.017

Table 5. **Ablation Study on the D-NeRF Dataset** [37]. Results show that incorporating the mask M to prevent the dilation of invisible Gaussians improves reconstruction quality. Furthermore, even when adjusting Mip-Splatting’s expansion scale to match the minimum dilation scale of our method, its performance remains inferior.

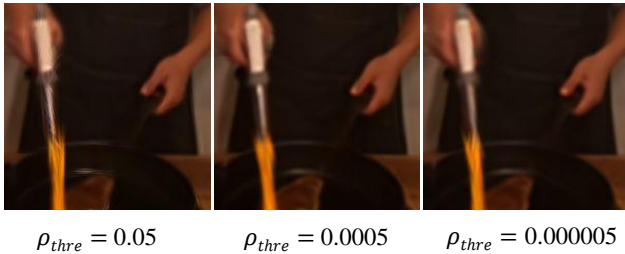


Figure 6. **Ablation Study on the Hyperparameter** ρ_{thre} : A lower ρ_{thre} imposes stricter frequency constraints on the Gaussian while reducing sensitivity to illumination variations.

show that D3DGS effectively captures deformation details at full resolution but introduces significant inflation artifacts when tested at lower sampling rates. After integrating Mip-Splatting, the capability of D3DGS to capture fine deformation details deteriorates. In contrast, our method maintains the original reconstruction quality of D3DGS and preserves more realistic scene details at lower resolutions.

5.3. Evaluation on N3DV dataset

Single-scale Training and Multi-scale Testing: To simulate zoom-in effects, we define the default resolution of 4DGaussians (1352×1014) as the full resolution. Models are trained on data downsampled by a factor of 4 and rendered at progressively higher resolutions (1×, 2×, and 4×). Following the approach used in the D-NeRF dataset, we integrate Mip-Splatting [56] into 4DGaussians as a baseline for comparison, ensuring consistency in the maximum sampling frequency computation between Mip-Splatting and our method. The results in Tab. 3 demonstrate that our method achieves anti-aliasing performance comparable to *Mip-Splatting* while effectively constraining the frequency of 4DGS, reducing redundant Gaussians, and improving reconstruction quality. As shown in Fig. 5, our approach preserves the ability of 4DGS to learn deformations but affects its sensitivity to lighting. This effect arises from the scales loss constraining the intrinsic scale of Gaussians, which can be mitigated by adjusting ρ_{thre} , a more in-depth analysis is provided in the supplementary materials.

5.4. Ablation Study

4D Scale-adaptive Filter: Compared with the 3D smoothing filter [56], the proposed 4D scale-adaptive filter has two advantages in 4DGS: (1) it prevents unnecessary splatting of invisible Gaussians, and (2) it preserves Gaussian anisotropy by adaptively adjusting splatting scales within a defined range. To validate these advantages, we integrate the masking operation M from Eq. (12) into Mip-Splatting to avoid splatting invisible Gaussians and set its fixed scale equal to the minimal adaptive scale $\rho_{min} \cdot \sigma_s$ used by the proposed method. Quantitative results in Tab. 5 demonstrate the effectiveness of the 4D scale-adaptive filter beyond merely using smaller splatting scales.

Scale Regularization: To validate the effectiveness of jointly employing the scale loss \mathcal{L}_{scales} and the 4D scale-adaptive filter for constraining frequencies of 4D Gaussians, we train models on the D-NeRF dataset [37], downsampled by a factor of 4, and evaluate rendering quality at progressively higher resolutions (1×, 2×, and 4×). Quantitative results are summarized in Tab. 4. Due to the negative impact of the D3DGS filter [55] on full-resolution reconstruction, we adopt a smaller minimum dilation ratio ρ_{min} , which, however, yields insufficient frequency constraints and poorer anti-aliasing compared to Mip-Splatting [56] at higher resolutions. By introducing \mathcal{L}_{scales} to regularize Gaussian scales during deformation, our approach effectively alleviates this limitation, achieving superior anti-aliasing performance over Mip-Splatting in monocular video reconstruction tasks.

6. Limitations

Our method is sensitive to the hyperparameter ρ_{thre} , which determines the critical scale at which Gaussians are prevented from dilation and subjected to scales loss constraints. As shown in Fig. 6, a smaller ρ_{thre} reduces 4DGS’s sensitivity to lighting, while a larger ρ_{thre} weakens frequency constraints on 4DGS. Additionally, if a Gaussian fails to deform accurately, scale regularization may enlarge redundant small Gaussians, leading to negative optimization.

7. Conclusion

We propose a maximum sampling frequency formulation for 4DGS and introduce the 4D Scale-Adaptive Filter and Scale Regularization to effectively constrain Gaussian frequencies. Experiments demonstrate that in monocular video reconstruction, our method eliminates severe artifacts caused by sampling rate changes without compromising reconstruction quality. In multi-view video reconstruction, it not only removes these artifacts but also significantly reduces redundant Gaussians, improving reconstruction quality.

References

- [1] Kurt Akeley. Reality engine graphics. In *Proceedings of the 20th annual conference on Computer graphics and interactive techniques*, pages 109–116, 1993. 2
- [2] Benjamin Attal, Jia-Bin Huang, Christian Richardt, Michael Zollhoefer, Johannes Kopf, Matthew O’Toole, and Changil Kim. Hyperreel: High-fidelity 6-dof video with ray-conditioned sampling. In *Proceedings of the IEEE/CVF Conference on Computer Vision and Pattern Recognition*, pages 16610–16620, 2023. 1
- [3] Jeongmin Bae, Seoha Kim, Youngsik Yun, Hahyun Lee, Gun Bang, and Youngjung Uh. Per-gaussian embedding-based deformation for deformable 3d gaussian splatting. In *European Conference on Computer Vision*, pages 321–335. Springer, 2024. 1, 2
- [4] Jonathan T Barron, Ben Mildenhall, Matthew Tancik, Peter Hedman, Ricardo Martin-Brualla, and Pratul P Srinivasan. Mip-nerf: A multiscale representation for anti-aliasing neural radiance fields. In *Proceedings of the IEEE/CVF international conference on computer vision*, pages 5855–5864, 2021. 2
- [5] Jonathan T Barron, Ben Mildenhall, Matthew Tancik, Peter Hedman, Ricardo Martin-Brualla, and Pratul P Srinivasan. Mip-nerf: A multiscale representation for anti-aliasing neural radiance fields. In *Proceedings of the IEEE/CVF international conference on computer vision*, pages 5855–5864, 2021. 5
- [6] Jonathan T Barron, Ben Mildenhall, Dor Verbin, Pratul P Srinivasan, and Peter Hedman. Zip-nerf: Anti-aliased grid-based neural radiance fields. In *Proceedings of the IEEE/CVF International Conference on Computer Vision*, pages 19697–19705, 2023. 2
- [7] Qizhi Chen, Delin Qu, Yiwen Tang, Haoming Song, Yiting Zhang, Dong Wang, Bin Zhao, and Xuelong Li. Freegaussian: Guidance-free controllable 3d gaussian splats with flow derivatives. *arXiv preprint arXiv:2410.22070*, 2024. 2
- [8] Xiaoxue Chen, Junchen Liu, Hao Zhao, Guyue Zhou, and Ya-Qin Zhang. Nerf: 3d reconstruction and view synthesis for transparent and specular objects with neural refractive-reflective fields. *arXiv preprint arXiv:2309.13039*, 2023. 1
- [9] Woong Oh Cho, In Cho, Seoha Kim, Jeongmin Bae, Youngjung Uh, and Seon Joo Kim. 4d scaffold gaussian splatting for memory efficient dynamic scene reconstruction. *arXiv preprint arXiv:2411.17044*, 2024. 1, 2
- [10] Franklin C Crow. Summed-area tables for texture mapping. In *Proceedings of the 11th annual conference on Computer graphics and interactive techniques*, pages 207–212, 1984. 2
- [11] Pinxuan Dai, Peiquan Zhang, Zheng Dong, Ke Xu, Yifan Peng, Dandan Ding, Yujun Shen, Yin Yang, Xinguo Liu, Rynson WH Lau, et al. 4d gaussian videos with motion layering. *ACM Transactions on Graphics (TOG)*, 44(4):1–14, 2025. 1
- [12] Michael Deering, Stephanie Winner, Bic Schediwy, Chris Duffy, and Neil Hunt. The triangle processor and normal vector shader: a vlsi system for high performance graphics. *Acm siggraph computer graphics*, 22(4):21–30, 1988. 2
- [13] Jiemin Fang, Taoran Yi, Xinggang Wang, Lingxi Xie, Xiaopeng Zhang, Wenyu Liu, Matthias Nießner, and Qi Tian. Fast dynamic radiance fields with time-aware neural voxels. In *SIGGRAPH Asia 2022 Conference Papers*, pages 1–9, 2022. 5
- [14] Sara Fridovich-Keil, Giacomo Meanti, Frederik Rahbæk Warburg, Benjamin Recht, and Angjoo Kanazawa. K-planes: Explicit radiance fields in space, time, and appearance. In *Proceedings of the IEEE/CVF Conference on Computer Vision and Pattern Recognition*, pages 12479–12488, 2023. 1, 5
- [15] Henry Fuchs, Jack Goldfeather, Jeff P Hultquist, Susan Spach, John D Austin, Frederick P Brooks Jr, John G Eyles, and John Poulton. Fast spheres, shadows, textures, transparencies, and image enhancements in pixel-planes. *ACM Siggraph Computer Graphics*, 19(3):111–120, 1985. 2
- [16] Mingju Gao, Yike Pan, Huan-ang Gao, Zongzheng Zhang, Wenyi Li, Hao Dong, Hao Tang, Li Yi, and Hao Zhao. Partrm: Modeling part-level dynamics with large cross-state reconstruction model. In *Proceedings of the Computer Vision and Pattern Recognition Conference*, pages 7004–7014, 2025. 1
- [17] Paul Haeberli and Kurt Akeley. The accumulation buffer: Hardware support for high-quality rendering. *ACM SIGGRAPH computer graphics*, 24(4):309–318, 1990. 2
- [18] Paul S Heckbert. Fundamentals of texture mapping and image warping. 1989. 2
- [19] Wenbo Hu, Yuling Wang, Lin Ma, Bangbang Yang, Lin Gao, Xiao Liu, and Yuewen Ma. Tri-miprf: Tri-mip representation for efficient anti-aliasing neural radiance fields. In *Proceedings of the IEEE/CVF International Conference on Computer Vision*, pages 19774–19783, 2023. 2
- [20] Wenbo Hu, Yuling Wang, Lin Ma, Bangbang Yang, Lin Gao, Xiao Liu, and Yuewen Ma. Tri-miprf: Tri-mip representation for efficient anti-aliasing neural radiance fields. In *Proceedings of the IEEE/CVF International Conference on Computer Vision*, pages 19774–19783, 2023. 5
- [21] Yi-Hua Huang, Yang-Tian Sun, Ziyi Yang, Xiaoyang Lyu, Yan-Pei Cao, and Xiaojuan Qi. Sc-gs: Sparse-controlled gaussian splatting for editable dynamic scenes. In *Proceedings of the IEEE/CVF conference on computer vision and pattern recognition*, pages 4220–4230, 2024. 1, 2
- [22] Yingwenqi Jiang, Jiadong Tu, Yuan Liu, Xifeng Gao, Xiaoxiao Long, Wenping Wang, and Yuexin Ma. Gaussian-shader: 3d gaussian splatting with shading functions for reflective surfaces. In *Proceedings of the IEEE/CVF Conference on Computer Vision and Pattern Recognition*, pages 5322–5332, 2024. 1
- [23] Bernhard Kerbl, Georgios Kopanas, Thomas Leimkühler, and George Drettakis. 3d gaussian splatting for real-time radiance field rendering. *ACM Trans. Graph.*, 42(4):139–1, 2023. 1, 2
- [24] Bernhard Kerbl, Georgios Kopanas, Thomas Leimkühler, and George Drettakis. 3d gaussian splatting for real-time radiance field rendering. *ACM Trans. Graph.*, 42(4):139–1, 2023. 3
- [25] Haolin Li, Jinyang Liu, Mario Sznajder, and Octavia Camps. 3d-hgs: 3d half-gaussian splatting. In *Proceedings of the*

- Computer Vision and Pattern Recognition Conference*, pages 10996–11005, 2025. 2
- [26] Jiameng Li, Yue Shi, Jiezhong Cao, Bingbing Ni, Wenjun Zhang, Kai Zhang, and Luc Van Gool. Mipmap-gs: Let gaussians deform with scale-specific mipmap for anti-aliasing rendering. In *2025 International Conference on 3D Vision (3DV)*, pages 935–945. IEEE, 2025. 2
- [27] Tianye Li, Mira Slavcheva, Michael Zollhoefer, Simon Green, Christoph Lassner, Changil Kim, Tanner Schmidt, Steven Lovegrove, Michael Goesele, Richard Newcombe, et al. Neural 3d video synthesis from multi-view video. In *Proceedings of the IEEE/CVF conference on computer vision and pattern recognition*, pages 5521–5531, 2022. 1
- [28] Tianye Li, Mira Slavcheva, Michael Zollhoefer, Simon Green, Christoph Lassner, Changil Kim, Tanner Schmidt, Steven Lovegrove, Michael Goesele, Richard Newcombe, et al. Neural 3d video synthesis from multi-view video. In *Proceedings of the IEEE/CVF conference on computer vision and pattern recognition*, pages 5521–5531, 2022. 5, 6, 7, 1, 2
- [29] Zhengqi Li, Simon Niklaus, Noah Snavely, and Oliver Wang. Neural scene flow fields for space-time view synthesis of dynamic scenes. In *Proceedings of the IEEE/CVF Conference on Computer Vision and Pattern Recognition*, pages 6498–6508, 2021. 1
- [30] Zhan Li, Zhang Chen, Zhong Li, and Yi Xu. Spacetime gaussian feature splatting for real-time dynamic view synthesis. In *Proceedings of the IEEE/CVF Conference on Computer Vision and Pattern Recognition*, pages 8508–8520, 2024. 1, 2
- [31] Junchen Liu, Wenbo Hu, Zhuo Yang, Jianteng Chen, Guoliang Wang, Xiaoxue Chen, Yantong Cai, Huan-ang Gao, and Hao Zhao. Rip-nerf: Anti-aliasing radiance fields with ripmap-encoded platonic solids. In *ACM SIGGRAPH 2024 Conference Papers*, pages 1–11, 2024. 2
- [32] Jiahao Lu, Jiacheng Deng, Ruijie Zhu, Yanzhe Liang, Wenfei Yang, Xu Zhou, and Tianzhu Zhang. Dn-4dgs: Denoised deformable network with temporal-spatial aggregation for dynamic scene rendering. *Advances in Neural Information Processing Systems*, 37:84114–84138, 2025. 1, 2
- [33] Abraham Mammen. Transparency and antialiasing algorithms implemented with the virtual pixel maps technique. *IEEE Computer Graphics and Applications*, 9(4):43–55, 1989. 2
- [34] Klaus Mueller, Torsten Moller, J Edward Swan, Roger Crawfis, Naeem Shareef, and Roni Yagel. Splatting errors and antialiasing. *IEEE Transactions on Visualization and Computer Graphics*, 4(2):178–191, 1998. 2
- [35] H NYQUIST. Certain topics in telegraph transmission theory. *AIEE Trans.*, 47:617–644, 1928. 2
- [36] Keunhong Park, Utkarsh Sinha, Peter Hedman, Jonathan T Barron, Sofien Bouaziz, Dan B Goldman, Ricardo Martin-Brualla, and Steven M Seitz. Hypernerf: A higher-dimensional representation for topologically varying neural radiance fields. *arXiv preprint arXiv:2106.13228*, 2021. 1
- [37] Albert Pumarola, Enric Corona, Gerard Pons-Moll, and Francesc Moreno-Noguer. D-nerf: Neural radiance fields for dynamic scenes. In *Proceedings of the IEEE/CVF conference on computer vision and pattern recognition*, pages 10318–10327, 2021. 5, 6, 7, 8, 1, 2, 3
- [38] Delin Qu, Qizhi Chen, Pingrui Zhang, Xianqiang Gao, Bin Zhao, Zhigang Wang, Dong Wang, and Xuelong Li. Livescene: Language embedding interactive radiance fields for physical scene control and rendering. In *The Thirty-eighth Annual Conference on Neural Information Processing Systems*, 2024. 1
- [39] Delin Qu, Chi Yan, Dong Wang, Jie Yin, Qizhi Chen, Dan Xu, Yiting Zhang, Bin Zhao, and Xuelong Li. Implicit event-rgb neural slam. In *Proceedings of the IEEE/CVF Conference on Computer Vision and Pattern Recognition (CVPR)*, pages 19584–19594, 2024. 1
- [40] Claude E Shannon. Communication in the presence of noise. *Proceedings of the IRE*, 37(1):10–21, 1949. 2
- [41] Ruizhi Shao, Zerong Zheng, Hanzhang Tu, Boning Liu, Hongwen Zhang, and Yebin Liu. Tensor4d: Efficient neural 4d decomposition for high-fidelity dynamic reconstruction and rendering. In *Proceedings of the IEEE/CVF Conference on Computer Vision and Pattern Recognition*, pages 16632–16642, 2023. 5
- [42] Richard Shaw, Michal Nazarczuk, Jifei Song, Arthur Moreau, Sibi Catley-Chandar, Helisa Dharmo, and Eduardo Perez-Pellitero. Swings: Sliding windows for dynamic 3d gaussian splatting. *arXiv preprint arXiv:2312.13308*, 2023. 1, 2
- [43] Xiaowei Song, Jv Zheng, Shiran Yuan, Huan-ang Gao, Jingwei Zhao, Xiang He, Weihao Gu, and Hao Zhao. Sags: Scale-adaptive gaussian splatting for training-free anti-aliasing. *arXiv preprint arXiv:2403.19615*, 2024. 2, 7
- [44] Jonathan Steuer. Defining virtual reality: dimensions determining telepresence. 1992. 1
- [45] J Edward Swan, Klaus Mueller, Torsten Moller, N Shareef, Roger Crawfis, and Roni Yagel. An anti-aliasing technique for splatting. In *Proceedings. Visualization'97 (Cat. No. 97CB36155)*, pages 197–204. IEEE, 1997. 2
- [46] Ethan Waisberg, Joshua Ong, Mouayad Masalkhi, Nasif Zaman, Prithul Sarker, Andrew G. Lee, and A. Tavakkoli. The future of ophthalmology and vision science with the apple vision pro. *Eye*, 38:242–243, 2023. 1
- [47] Nan Wang, Yuantao Chen, Lixing Xiao, Weiqing Xiao, Bohan Li, Zhaoxi Chen, Chongjie Ye, Shaocong Xu, Saining Zhang, Ziyang Yan, et al. Unifying appearance codes and bilateral grids for driving scene gaussian splatting. *arXiv preprint arXiv:2506.05280*, 2025. 1
- [48] Turner Whitted. An improved illumination model for shaded display. In *ACM Siggraph 2005 Courses*, pages 4–es. 2005. 2
- [49] Lance Williams. Pyramidal parametrics. In *Proceedings of the 10th annual conference on Computer graphics and interactive techniques*, pages 1–11, 1983. 2
- [50] Guanjin Wu, Taoran Yi, Jiemin Fang, Lingxi Xie, Xiaopeng Zhang, Wei Wei, Wenyu Liu, Qi Tian, and Xinggang Wang. 4d gaussian splatting for real-time dynamic scene rendering. In *Proceedings of the IEEE/CVF conference on computer vision and pattern recognition*, pages 20310–20320, 2024. 1, 2, 3, 5, 6

- [51] Chi Yan, Delin Qu, Dan Xu, Bin Zhao, Zhigang Wang, Dong Wang, and Xuelong Li. Gs-slam: Dense visual slam with 3d gaussian splatting. In *Proceedings of the IEEE/CVF Conference on Computer Vision and Pattern Recognition (CVPR)*, pages 19595–19604, 2024. [1](#)
- [52] Jing-Wen Yang, Jia-Mu Sun, Yong-Liang Yang, Jie Yang, Ying Shan, Yan-Pei Cao, and Lin Gao. Dmit: Deformable mipmapped tri-plane representation for dynamic scenes. In *European Conference on Computer Vision*, pages 436–453. Springer, 2024. [5](#), [7](#)
- [53] Runyi Yang, Zhenxin Zhu, Zhou Jiang, Baijun Ye, Xiaoxue Chen, Yifei Zhang, Yuantao Chen, Jian Zhao, and Hao Zhao. Spectrally pruned gaussian fields with neural compensation. *arXiv preprint arXiv:2405.00676*, 2024. [1](#), [2](#)
- [54] Zeyu Yang, Hongye Yang, Zijie Pan, and Li Zhang. Real-time photorealistic dynamic scene representation and rendering with 4d gaussian splatting. *arXiv preprint arXiv:2310.10642*, 2023. [1](#), [2](#)
- [55] Ziyi Yang, Xinyu Gao, Wen Zhou, Shaohui Jiao, Yuqing Zhang, and Xiaogang Jin. Deformable 3d gaussians for high-fidelity monocular dynamic scene reconstruction. In *Proceedings of the IEEE/CVF conference on computer vision and pattern recognition*, pages 20331–20341, 2024. [1](#), [2](#), [3](#), [5](#), [6](#), [7](#), [8](#)
- [56] Zehao Yu, Anpei Chen, Binbin Huang, Torsten Sattler, and Andreas Geiger. Mip-splatting: Alias-free 3d gaussian splatting. In *Proceedings of the IEEE/CVF conference on computer vision and pattern recognition*, pages 19447–19456, 2024. [2](#), [3](#), [5](#), [6](#), [7](#), [8](#), [1](#)
- [57] Shiran Yuan and Hao Zhao. Slimmerf: Slimmable radiance fields. In *2024 International Conference on 3D Vision (3DV)*, pages 64–74. IEEE, 2024. [1](#)
- [58] Matthias Zwicker, Hanspeter Pfister, Jeroen Van Baar, and Markus Gross. Ewa volume splatting. In *Proceedings Visualization, 2001. VIS'01.*, pages 29–538. IEEE, 2001. [2](#), [3](#)

Alias-free 4D Gaussian Splatting

Supplementary Material

Abstract

This supplementary material accompanies the main paper by providing more details for reproducibility as well as additional evaluations and qualitative results to verify the effectiveness and robustness of Alias-free-4DGS:

▷ **Sec. 8:** Additional implementation details.

▷ **Sec. 9:** Additional experimental results, including more detailed view synthesis quality comparison, rendering visualization at multiple scales.

8. Implementation Details

For monocular video reconstruction, we adopt D3DGS [55], the state-of-the-art method, as our codebase. Similar to Mip-Splatting [56], we implement a coarse minimum sampling interval estimation Eq. (9) and a 4D scale-adaptive filter in PyTorch, while a more accurate minimum sampling interval update Eq. (10) and a 2D Mip Filter [56] are implemented in CUDA. During the initial 3k iterations, we train only the 3D Gaussians to achieve stable positions and shapes. Subsequently, joint optimization of 3D Gaussians and the deformation field is performed. The minimum sampling interval \hat{T}_k is computed using Eq. (9) for the first 6k iterations and then refined with Eq. (10). The maximum sampling frequency is the inverse of Eq. (10), ensuring consistency with D3DGS. The total training consists of 40k iterations.

For multi-view video reconstruction, we adopt 4DGaussian [50], another deformation-based approach, as our codebase, with minimal modifications except for the incorporation of an averaging operation using $M1$ in the scale loss Eq. (14). Following 4DGaussian, we train only the 3D Gaussians for the first 3k iterations to stabilize their positions and shapes before optimizing the deformation field. Given the severe overfitting of 4DGaussian on the N3DV dataset [28], we limit the deformation field training to 20k iterations, evaluating every 1k iterations to select the best checkpoint for final assessment. Notably, all models in our experiments follow this protocol to ensure fair comparisons.

9. Additional Experimental Results

Single-scale Training and Multi-scale Synthesis on the D-NeRF [37] dataset. As shown in Fig. 7, we train all methods on full-resolution images and evaluate them at scale $1\times$ and scale $1/4$ to simulate zoom-out effects. Both 4DGS with Mip-filter and Mip-Splatting [56] exhibit noticeable blurring and inflation artifacts at lower resolutions, especially in the Hell Warrior scene. While D3DGS [55]

captures fine deformation details at full resolution, it introduces significant inflation artifacts at lower resolutions. In contrast, our method maintains the original reconstruction quality of D3DGS and preserves more realistic scene details at lower resolutions.

Single-Scale Training and Multi-Scale Evaluation on the N3DV Dataset [28]. In the main text, we conducted simulated upscaling experiments on the N3DV dataset [28]. Here, we further perform simulated downscaling experiments. Table 6 presents the quantitative results, showing that constraining Gaussian frequency reduces redundant Gaussians and slightly improves reconstruction quality. While our method demonstrates comparable anti-aliasing capabilities to Mip-Splatting [56], its full-resolution reconstruction quality is slightly lower than expected.

We analyze potential reasons for this discrepancy. In multi-view video reconstruction, the presence of redundant Gaussians, inaccurate motion modeling, and limited adaptability of Gaussian deformation may contribute to this outcome. Our proposed scales loss is designed to constrain visible Gaussians; however, if a Gaussian fails to deform correctly and become invisible, scales loss may act as a negative optimization. In contrast, Mip-Splatting applies large-scale dilation filtering, which significantly reduces Gaussian opacity after rendering and is less affected. Since scales loss does not regulate transparency, it may lead to small redundant Gaussians expanding instead of disappearing, resulting in adverse optimization effects.

Single-Scale Training and Multi-Scale Rendering on the D-NeRF Dataset [37]. We conduct additional experiments on the D-NeRF dataset [28] to evaluate the performance of our method at different scales. As shown in Fig. 8, we train all models on images downsampled by a factor of four and render them at full resolution to simulate zoom-in and moving-closer effects. Our method effectively eliminates high-frequency artifacts and produces more complete object shapes compared to other methods. In contrast, D3DGS [55] exhibits noticeable blurring and inflation artifacts. D3DGS [55] integrating Mip-Splatting [56] and the 2D Mip filter achieves better visual fidelity but exhibits numerous high-frequency artifacts. In addition, Mip-Splatting [56] fails to capture fine details in dynamic reconstruction and produces incomplete object shapes.

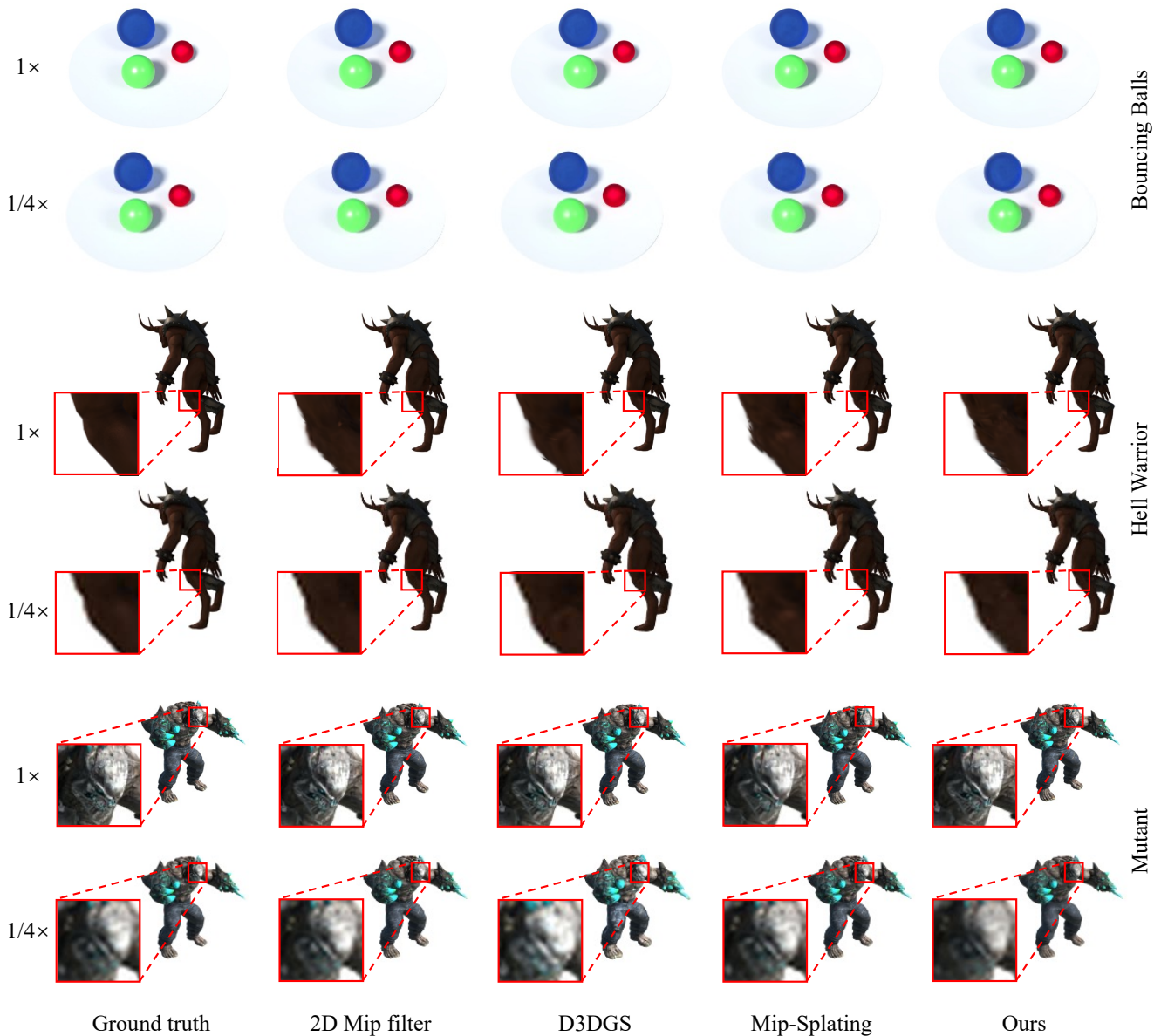
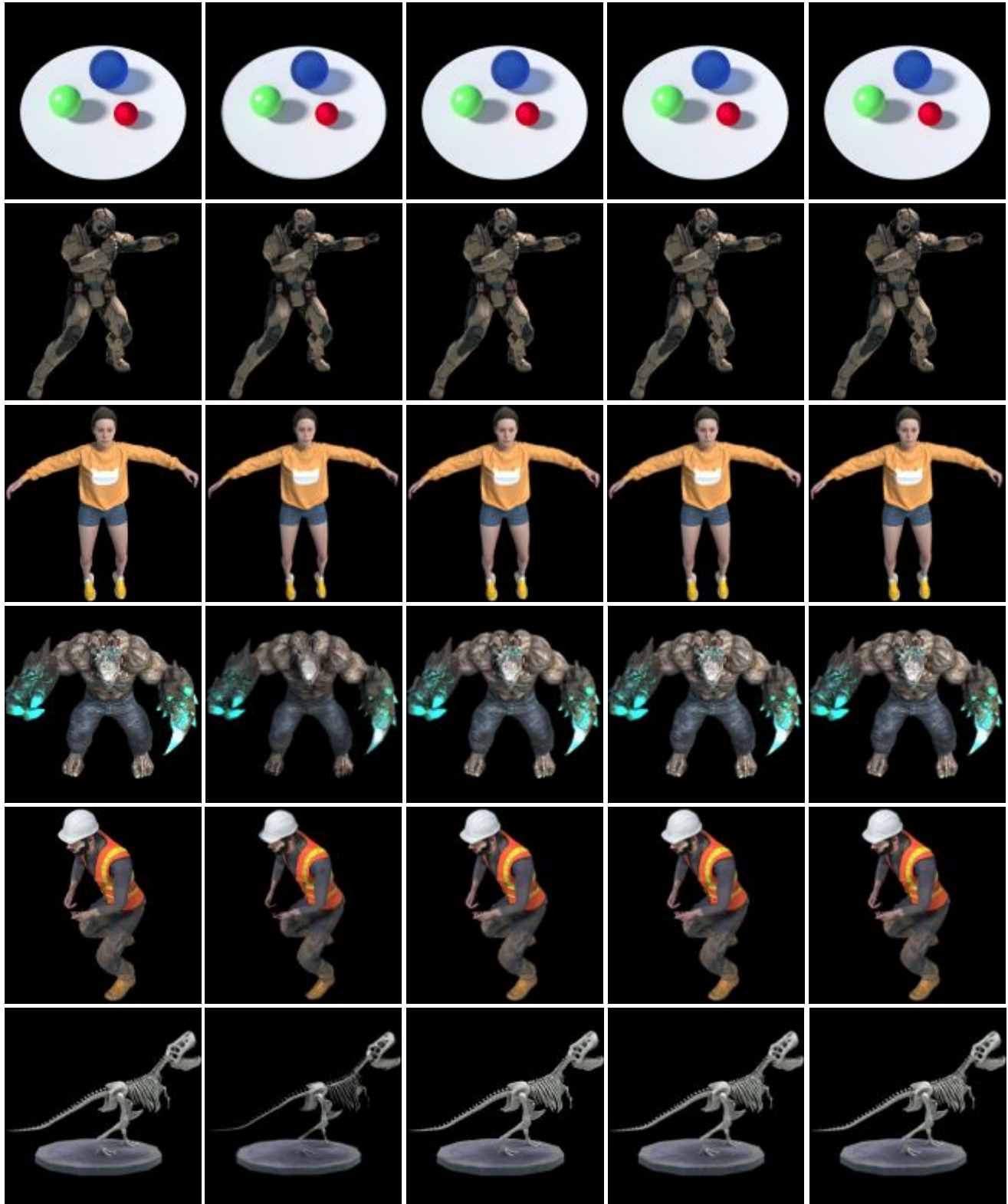


Figure 7. Single-scale Training and Multi-scale Synthesis on the D-NeRF dataset [37]. All methods are trained at full resolution and evaluated at various lower resolutions to simulate zoom-out effects. D3DGS [55] exhibits noticeable blurring and inflation artifacts at lower resolutions. Integrating Mip-splatting [56] mitigates inflation but introduces local reconstruction distortions. In contrast, our method preserves the reconstruction quality of D3DGS while maintaining more realistic visual fidelity at lower resolutions.

Methods	PSNR \uparrow					SSIM \uparrow					LPIPS \downarrow					\mathcal{G}
	Full Res.	1/2 Res.	1/4 Res.	1/8 Res.	Avg.	Full Res.	1/2 Res.	1/4 Res.	1/8 Res.	Avg.	Full Res.	1/2 Res.	1/4 Res.	1/8 Res.	Avg.	
4DGaussian [50] *	31.56	29.49	25.99	22.46	27.38	0.938	0.916	0.858	0.763	0.869	0.148	0.106	0.094	0.124	0.118	125k
2D Mip Filter [56]	31.66	32.06	31.90	30.50	31.53	0.936	0.945	0.955	0.950	0.946	0.150	0.096	0.045	0.032	0.081	103k
Mip-Splatting _{4D} [56]	31.86	32.35	32.57	31.54	32.08	0.937	0.945	0.956	0.955	0.948	0.155	0.099	0.047	0.031	0.083	94k
Ours	31.75	32.22	32.35	31.28	31.90	0.937	0.946	0.957	0.955	0.949	0.154	0.099	0.047	0.031	0.083	92k

Table 6. Single-Scale Training and Multi-Scale Evaluation on the N3DV Dataset [28].



Ground-truth

D3DGS

2D Mip Filter

Mip-Splatting

Ours

Figure 8. **Single-Scale Training and Multi-Scale Synthesis on the D-NeRF dataset [37]**. All models are trained on images downsampled by a factor of four and rendered at full resolution to simulate zoom-in. Our method effectively eliminates high-frequency artifacts and produces more complete object shapes compared to Mip-Splatting.